


Cite this: *Energy Environ. Sci.*,
2024, 17, 5542

Ameliorated trap density and energetic disorder via a strengthened intermolecular interaction strategy to construct efficient non-halogenated organic solar cells†

Shenzheng Gao,^a Yimin Zhang,^{bcd} Seonghun Jeong,^e Xinjie Zhou,^a Hao Xu,^a Shanlei Xu,^a Daqiang Chen,^{cd} Wenzhu Liu,^f Changduk Yang,^g  *^{eg} Sheng Meng,^{*cdh} Weiguo Zhu ^a and Xin Song ^{*ai}

In light of environmental considerations, non-halogenated solvent casting is of critical importance for the commercialization of organic solar cells (OSCs). However, the severe traps and energetic disorder induced by the uncontrollable aggregation and anisotropic packing distribution in photoactive layers treated with non-halogenated solvents significantly limit the photovoltaic performance. In this work, a strengthened intermolecular interaction (SII) strategy is proposed, in which a non-halogenated dibenzyl ether (DBE) additive is developed and incorporated into non-halogenated OSC devices. The functional oxygen atom in the DBE molecule, together with the planar and rigid configuration, can induce collaborative hydrogen-bond and π - π intermolecular interaction with acceptors to construct a polycrystalline structure and further trigger the pre-aggregation process in the liquid-solid transition period. Consequently, the SII treatment can induce enhanced crystallinity and more favorable molecular orientation simultaneously, which can ameliorate the detrimental energetic disorder and efficiently elevate the carrier generation rate and transport, in addition to the diminished trap densities. Thus, the efficiency of non-halogenated OSC is upgraded from 17.1% to 19.4% after SII treatment, marking one of the highest performances for non-halogenated OSC devices. More strikingly, the roll-off of photovoltaic performance under the thick-film condition is appreciably mitigated, with a champion efficiency of 17.4% being achieved when the thickness reaches 300 nm, representing the superiority of SII strategy in the construction of eco-friendly, efficient, and thickness-insensitive OSCs.

Received 18th January 2024,
Accepted 11th June 2024

DOI: 10.1039/d4ee00291a

rsc.li/ees

Broader context

Most of recent high-performance organic solar cells (OSCs) require the use of toxic halogenated solvents in the device preparation process, which greatly limits the industrial development of the OSCs. Therefore, a series of non-halogenated solvents have been developed to fabricate non-halogenated devices. However, the high boiling points of these solvents induce anisotropic molecular aggregation and distinct donor-acceptor phase separation during the long-term film-forming process, resulting in severe energetic disorder and trap defects, which significantly restrict the enhancement of power conversion efficiency (PCE). The molecular packing and microscopic phase separation in the bulk heterojunctions are strongly dependent on the precise intermolecular interactions. Herein, we have developed a strengthened intermolecular interaction (SII) strategy by introducing the non-halogenated solvent additive dibenzyl ether (DBE) in the active layer. The functional oxygen atoms in the DBE structure can form hydrogen-bond interactions with the dithienothiophen[3.2-b]pyrrolobenzothiadiazole (BTP) core unit. More critically, the planar and rigid configuration of the additive DBE can form the tight π - π interactions with the acceptor block. Benefiting from the above advantages, the optimized DBE device can harvest a champion PCE of 19.4% with an increase of 13.4% in comparison to the control device based on neat toluene solvent (17.1%).

^a School of Materials Science and Engineering, Jiangsu Engineering Laboratory of Light-Electricity-Heat Energy-Converting Materials and Applications, Changzhou University, Changzhou 213164, P. R. China. E-mail: xin.song@cczu.edu.cn

^b Key Laboratory of Materials Physics, Ministry of Education, School of Physics, Zhengzhou University, Zhengzhou 450001, China

^c Beijing National Laboratory for Condensed Matter Physics and Institute of Physics, Chinese Academy of Sciences, Beijing 100190, P. R. China. E-mail: smeng@iphy.ac.cn

^d School of Physical Sciences, University of Chinese Academy of Sciences, Beijing 100049, P. R. China

^e School of Energy and Chemical Engineering, Perovtronics Research Center, Low Dimensional Carbon Materials Center, Ulsan National Institute of Science and Technology (UNIST), Ulsan 44919, South Korea. E-mail: yang@unist.ac.kr

^f Research Center for New Energy Technology, Shanghai Institute of Microsystem and Information Technology, Chinese Academy of Sciences, Shanghai 201800, China

^g Graduate School of Carbon Neutrality, Ulsan National Institute of Science and Technology (UNIST), Ulsan 44919, South Korea

^h Songshan Lake Materials Laboratory, Dongguan, Guangdong 523808, P. R. China

ⁱ Key Laboratory of Advanced Energy Materials Chemistry (Ministry of Education), Nankai University, Tianjin 300071, P. R. China

† Electronic supplementary information (ESI) available. See DOI: <https://doi.org/10.1039/d4ee00291a>

1. Introduction

The cooperative feasibility of high-throughput solution manufacturing, flexibility and semi-transparency in organic solar cells (OSCs) has inspired decades of vigorous explorations for their potential applications. The recent success in non-fullerene acceptor (NFA) development has enabled lab-scale OSCs to achieve high power conversion efficiency (PCE) surpassing 20%.^{1–3} Typically, these high-efficiency devices are fabricated using halogenated solvent on the basis that the halogen atoms can form various intermolecular interactions (such as hydrogen-bond, halogen-bond, and halogen- π interactions) with either donors or acceptors to further regulate the film-formation kinetics of the photoactive bulk heterojunction (BHJ) layer.^{4–6} Unfortunately, these halogenated solvents exhibit toxicity and cause damage to the human body and natural environment, which remarkably restrict their actual industrialization potential. In light of this, various non-halogenated solvents, such as toluene, *ortho*-xylene (*o*-XY), *para*-xylene (*p*-XY) and 1,2,4-trimethylbenzene (TMB), have been explored to construct environmentally friendly organic solar cells.^{7–9} However, the lack of the fine intermolecular interactions mentioned above critically resulted in an uncontrollable molecule assembly process in BHJ films treated with non-halogenated solvents, which would induce detrimental carrier traps in the BHJ film and further reduce the power conversion efficiency (PCE) of the solar cells.

To tackle this problem, the fine-tuning of alkyl sidechains has been developed as a strategy to enhance the intermolecular interactions of the target NFA molecules. For example, Li *et al.* synthesized a new molecule (named BTO) by substituting the alkyl sidechain in the Y-series acceptor with an oligo(ethylene glycol) (OEG) chain.¹⁰ After introducing BTO into the original binary blend as a third component, the hydrogen-bond interaction introduced by the OEG chain can manipulate the assembly packing in the BHJ blend film, which provides enhanced photovoltaic performance and operational stability simultaneously. Furthermore, Huang *et al.* reported that the asymmetric alkyl chain distribution in the inner bay of Y-series acceptors can bring about a dipole interaction, which can promote the molecular crystallinity and guarantee the favorable hierarchical morphology.^{11,12} Nevertheless, the asymmetric or fundamental alkyl chain would unavoidably increase the synthesis and purification cost of the NFA molecules, which is not economical for the industrialization of OSCs. More critically, the flexible alkyl chain cannot easily regulate the molecular packing orientation of dithienothiophen[3.2-*b*]pyrrolobenzothiadiazole (BTP) based NFA materials, resulting in the widespread existence of disordered and chaotic accumulation phenomenon in BHJ films, which in turn leads to severe energy disorder (>30 meV) with elevated trap density ($>3 \times 10^{16}$ cm⁻³) and further weakened charge generation, transport and collection capabilities.^{13–15} Therefore, according to the reports in the literature, the photovoltaic performance based on non-halogenated OSC is limited to 19.0%, which lags behind that of halogenated solvent casted OSCs (20.1%). As consequence, it is urgent to develop a straightforward and promising approach to modulate the packing orientation and crystallinity of fused-ring

BTP core units to ameliorate the severe energetic disorder and trap generation behavior of non-halogenated OSCs for real commercialization.

Solvent additive engineering is extensively adapted to regulate energy disorder behavior. However, most of the reported additives intrinsically contain halogens, which do not meet the environmental requirements. More critically, there is rarely systemic research on the development of productively non-halogenated additives adapted to fabricate high-efficiency non-halogenated OSCs. Herein, by introducing a low-cost, multifunctional non-halogenated dibenzyl ether (DBE) solvent additive into the BHJ layer, we propose a strengthened intermolecular interaction (SII) strategy to inhibit the energetic disorder behavior inside the non-halogenated OSC devices. The oxygen atoms in the DBE additive, together with the planar and stiff configuration, can concurrently induce durable hydrogen-bond and π - π intermolecular interactions in the BTP core block to trigger a highly-ordered polycrystalline structure, which could induce the pre-aggregation of the acceptor to facilitate the crystallinity and preferable face-on orientation. Undoubtedly, this unique SII strategy can amplify the carrier transport capability, diminish energetic disorder and diminish the trap density value. Benefitting from the above superiorities, the optimized DBE device can harvest a champion PCE of 19.4% with an increase of 13.4% in comparison with that of the control device based on neat toluene solvent (17.1%), representing one of the highest PCE values for non-halogenated OSC devices. More strikingly, the coherent morphology regulation would facilitate the mitigation of the roll-off of photovoltaic performance under increased film thickness, with a best PCE of 17.4% being harvested when the active layer thickness is increased to 300 nm.

2. Results and discussion

Regulating the aggregation behavior of acceptors

Toluene was selected as the host solvent. The PM6:BTP-eC9 system was chosen as the BHJ film; the chemical structures are depicted in Fig. 1a and b, respectively. As the aggregation behavior of the acceptor molecule plays a vital role in the BHJ blend morphology, especially for films processed with non-halogenated solvent, the main discussion focus is the effect of the additive on the BP-eC9 molecule. One of the main reasons we chose DBE is that it contains oxygen atoms from a structural point of view (shown in Fig. 1c). As reported by Li and Ying *et al.*, the strong electronegativity would induce a hydrogen-bond interaction force, which can create tight packing with adjacent molecules.^{10,15} Therefore, we believe that the presence of sulfur, nitrogen, and oxygen atoms in the BTP core unit might lead to the formation of multi-channel hydrogen bonds with the oxygen atoms on the additive DBE. To validate this hydrogen-bond interaction between DBE and BTP-eC9, Fourier-transform infrared spectroscopy (FT-IR) was implemented to track the wavenumber shift of the stretching peak. As illustrated in Fig. S1 (ESI[†]), based on our previous results, the peak in the range of 2900–3000 cm⁻¹ is attributed to the -CH₂- bond in the BTP core unit,¹⁶ which can be the representative signal of the

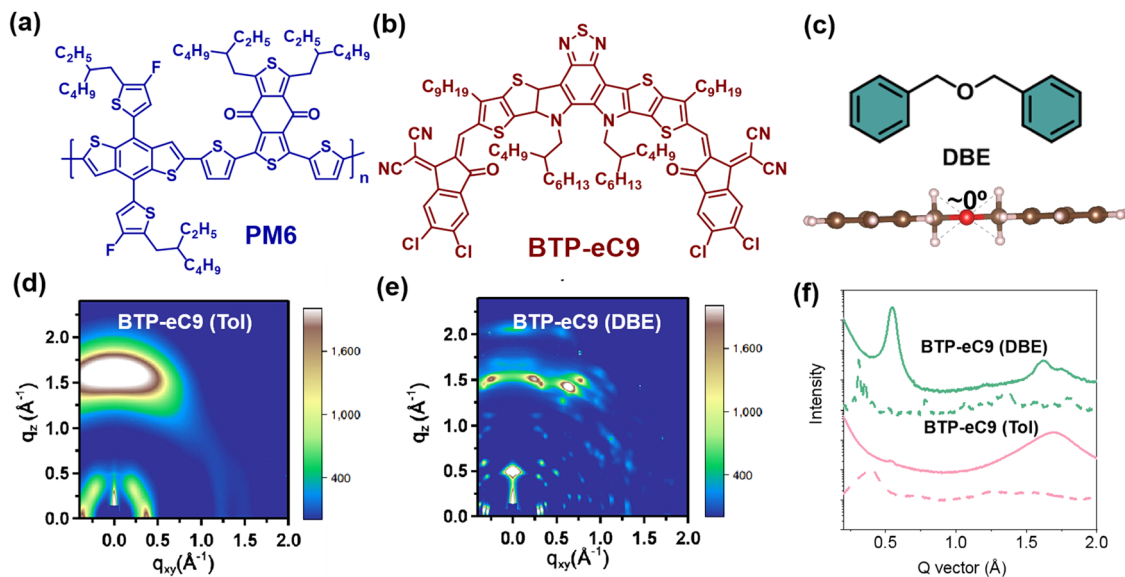


Fig. 1 Chemical structures of PM6 (a), BTP-eC9 (b), and the ether additive (c). 2D GIWAXS patterns of the BTP-eC9 neat film (d) and with the addition of DBE (e). (e) In-plane and out-of-plane profiles of corresponding 2D GIWAXS patterns. The pink curves are extracted from the GIWAXS profile of BTP-eC9 casted using neat toluene solvent. The green curves are extracted from the GIWAXS profile of BTP-eC9 casted using toluene solvent with the additive DBE. The solid lines represent the out-of-plane direction. The dashed lines represent the in-plane direction.

interaction between DBE additive and BTP core block. Consistent with the above conjecture, the stretching vibration of the CH_2 -group presents a pronounced shift from 2902 cm^{-1} to 2918 cm^{-1} after the incorporation of DBE, which reinforces the enhanced interaction with BTP-eC9 owing to the hydrogen-bond effect.

Conversely, as shown in Fig. 1c, according to density function theory (DFT) simulation, the methyl chain inserted into the benzene ring can eliminate the steric hindrance between the benzene rings, with the dihedral angle between two benzene rings being close to 0° , verifying the planar and rigid framework of the DBE molecules. Normally, this stiff configuration might induce a remarkable π - π interaction impact with large fused-ring molecules. Therefore, to evaluate this interaction, the adsorption energy (E_{ad}) was calculated using molecular dynamics (MD) simulation.¹⁷ As reported by Wang *et al.*, there are three packing models (S1, S2, W) for the BTP-series molecules according to single crystal analysis.¹⁸ Therefore, we tried to let the DBE molecule adsorb to each of these three configurations. As shown in Fig. S2–S4 (ESI[†]), we found that DBE had the lowest energy value (E_{ad} : -1.05 eV) when adsorbed to the W configuration with the largest overlapping area, whereas the E_{ad} values for S1 and S2 are -0.84 eV and -0.86 eV , respectively, indicating that the large-plane and rigid DBE molecules induce a tighter arrangement of molecules. This phenomenon can also be supported by the calculated molecular distance. As shown in Fig. S5 and S6 (ESI[†]), the distance between the BTP-eC9 molecules is $\sim 4.4\text{ \AA}$ as calculated by the MD simulation results. In contrast, the distance consequently drops to 2.9 \AA when the DBE molecule is adsorbed, which further proves the robust regulatory effect of the rigid DBE molecule on the BTP-eC9 molecule.

The above results were based on theoretical simulations; the manipulation of the organized arrangement by the additive

DBE was further confirmed from experimental results. It is worth mentioning that as the best device performance is obtained with the incorporation of a 0.5% volume ratio of the additive (as will be discussed in the photovoltaic performance part), we used this ratio for follow-up experimental characterization. Firstly, UV-Vis absorption spectroscopy was applied to intuitively justify the molecular aggregation property of the BTP-eC9 film without and with the additive DBE. As shown in Fig. S7a (ESI[†]), benefitting from the synergetic hydrogen-bond and π - π intermolecular interactions, it is apparent that the addition of DBE facilitates a distinct red-shift from 835 nm to 842 nm , which is also apparent in Fig. S7b (ESI[†]) for the PM6:BTP-eC9 blend film. More critically, when DBE is incorporated into the BTP-eC9, prominently reinforced vibronic shoulder peaks and a broadened absorption band are observed in the range from 600 – 800 nm , which represents further evidence of the unique aggregation behavior caused by the enhancement of intermolecular arrangement after the addition of DBE.¹⁹

This altered molecular ordering after the incorporation of the additive DBE was further validated using grazing-incidence X-ray wide-angle scattering (GIWAXS) measurement.^{20,21} As shown in Fig. 1d and Table S1 (ESI[†]), the preferential face-on orientation for BTP-eC9 is evidenced by the (010) peak in the out-of-plane (OOP) direction at $q_z = 1.69\text{ \AA}^{-1}$ with a crystallite coherence length (CCL, calculated using the Scherrer equation) of 2.16 nm . However, as shown in Fig. 1e and f, a number of diffraction peaks are observed in the GIWAXS image of DBE-treated BTP-eC9 film. This result clearly illustrates that the prominent π - π interaction can assist the BTP-eC9 to form the polycrystalline structure, which is obvious evidence of the tight intermolecular interaction between DBE and BTP-eC9 and is in good accordance with the UV-vis spectroscopy and simulation results.²²

Blend morphology

Generally, the adjustment of the molecular aggregation state has a crucial impact on the film-formation kinetics of BHJ film, which can be investigated using synergetic *in situ* photoluminescence (PL) and light scattering (LS) spectra.^{23,24} In this discussion, PM6:BTP-eC9 casted using neat toluene solvent is referred to as Tol, while blend films casted using mixed solvent and additive are abbreviated as DBE, respectively. It is worth mentioning that as the additive mainly acts on the acceptors, these *in situ* experiments are designed to collect the PL and LS signals under a 720 nm excitation laser during the spin-coating period. The film-formation process of the bulk heterojunction blend film (BHJ) involves three stages: solvent evaporation, liquid–solid transition, and subsequent growth towards the interpenetrated network.^{4,25} The 2D PL counter (750–900 nm) of PM6:BTP-eC9 blend film formation without and with the additive DBE are presented in Fig. 2a and b, and PL curves with the respect to the spinning time are summarized in Fig. S8 and S9 (ESI[†]), respectively.

In detail, in the first stage of the host solvent evaporation, the positions of the PL peaks for the acceptor in the PM6:BTP-eC9 without and with SII treatment show a similar tendency. However, in the liquid–solid transition stage (stage II), the intensity becomes weak due to the start of the BTP-eC9 aggregation and further prompts the closer distance between BTP-eC9 and PM6 molecules.²⁶ In particular, as presented in Fig. S10 (ESI[†]), the toluene-casted device exhibits a liquid–solid transition time of 70 ms, whereas that with the aromatic additive DBE with π – π interaction features earlier assembly of BTP-eC9 and a faster aggregation transition with a shortened LS phase transition time of 60 ms. This distinct action evidently indicates that the intermolecular interaction assisted by the additive DBE would

compress the transition time, which is beneficial for inhibiting chaotic packing direction during the film-forming process.

As the temporal intensity evolution extracted from the LS counters is the specific signal of molecule aggregation, we then utilized the *in situ* LS measurement to extract the domain size during the spin-coating period.²⁷ As highlighted in Fig. 2c of the LS intensity tracking at 720 nm with respect to the casting time, there is increased intensity from the solution to thin-film period (time range: 10–50 ms) after the DBE additive incorporation. Taken together with the *in situ* PL result, this enlarged signal in the solution state clearly suggests a favorable pre-aggregation process occurs in the PM6:BTP-eC9 solution after incorporation of the additive, which is induced by the favorable π – π molecular interaction between the additive and acceptor.²⁸ We believe that this pre-aggregation would act as a seed or nucleus center to guide the molecules to self-assemble with ordered packing and the preferred orientation, which aligns well with the quicker L–S transition time in the *in situ* PL measurements. Furthermore, this pre-aggregation behavior would convert the aggregate kinetics from 0.0464 s^{-1} (Tol), to 0.0875 s^{-1} (DBE). Additionally, due to these enhanced aggregation kinetics, there is a 1.5-fold increment in the LS intensity in the film-formation period especially for the DBE case. These two advantages are beneficial to construct the highly ordered crystallites in the DBE-treated film (demonstrated through GIWAXS characterization below).

Film morphology measurement

The above film-formation kinetics are strongly correlated with the crystallinity and microstructures of the blend films, which can be investigated using GIWAXS measurements.^{29,30} Fig. 3a and b depict the 2D GIWAXS diffraction patterns, while the

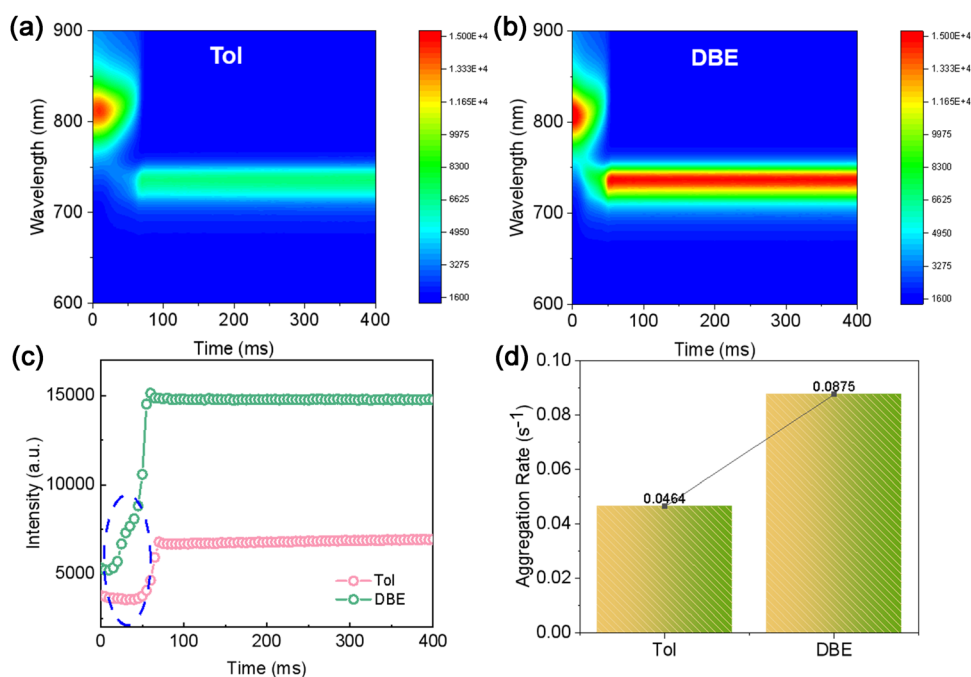


Fig. 2 *In situ* PL and LS counter of PM6:BTP-eC9 casted using neat toluene solvent (a) and with the additive DBE (b). (c) LS intensity as a function of spin time; (d) summary of aggregation rate during the film-formation period.

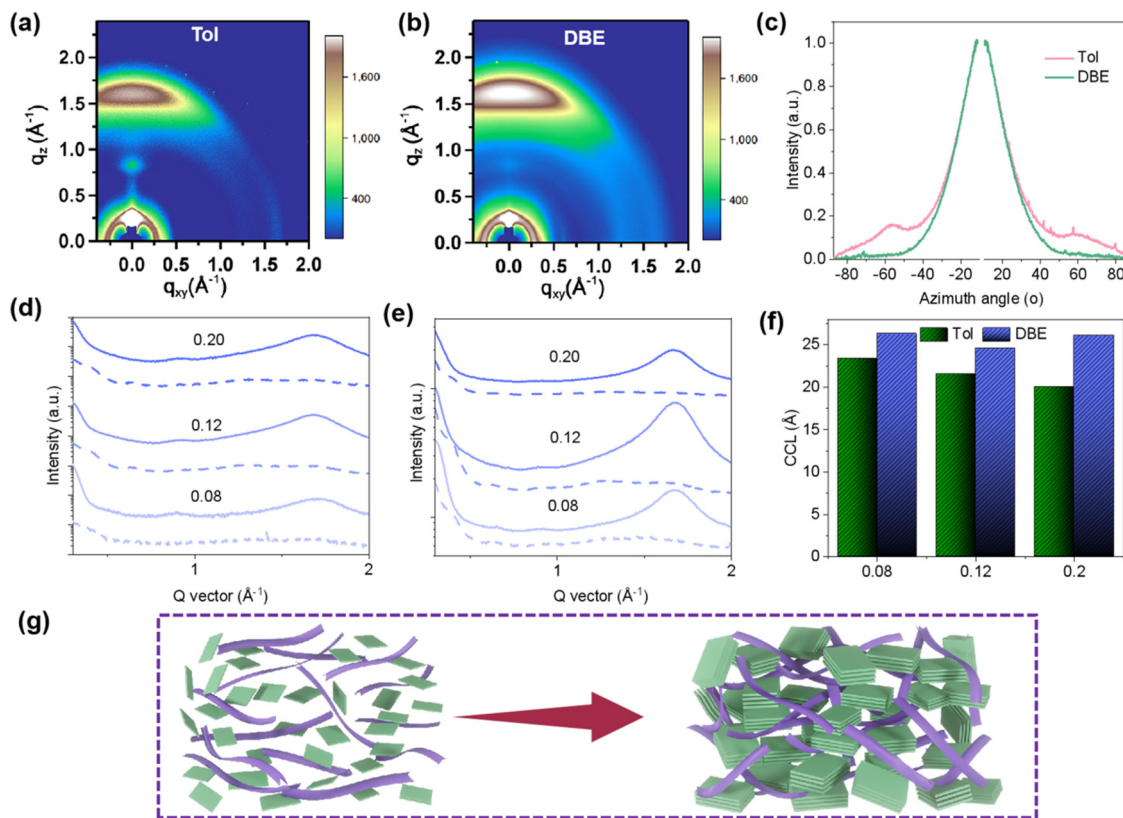


Fig. 3 2D GIWAXS patterns of PM6:BTP-eC9 casted using neat toluene solvent (a) and with the incorporation of the additive DBE (b). (c) Azimuth angle of the OOP (010) peak for the blend films without and with DBE incorporation. IP and OOP profiles with increased incident angles based on the PM6:BTP-eC9 film casted using neat toluene solvent (d) and with the incorporation of the additive DBE (e). (f) CCL calculated from the OOP (010) peak based on thick PM6:BTP-eC9 film without and with DBE additive. (g) Schematic diagram of the SII strategy in the morphological evolution.

line-cut profiles of the blend films are presented in Fig. S11 (ESI[†]), and corresponding crystallinity parameters are summarized in Table S2 (ESI[†]). In the out-of-plane (OOP) direction, there is insubstantial change in the location of the (010) diffraction peak of the PM6:BTP-eC9 without and with DBE additive treatment (both at 1.69 \AA^{-1}). However, the CCL in the (010) OOP direction is increased from 21.2 \AA (Tol) to 25.5 \AA (DBE), exhibiting the enhanced crystallinity with DBE treatment. In addition to the molecular packing, the orientation is a vital factor for the inhibition of energetic disorder phenomena. Therefore, a pole figure along the (010) OOP π - π stacking arc was plotted by extracting the integrated intensity as a function of the azimuth angles. Normally, the ranges of 0° - 45° and 45° - 90° are separately defined as the edge-on and face-on orientations, respectively.³¹ As presented in Fig. 3c, the slight shoulder peak at 45° - 90° indicates that the isotropic distribution is apparent in the neat-toluene-casted blend film, which would hinder the carrier transport and induce serious carrier trap recombination in the blend film. On the contrary, this shoulder disappeared with the introduction of the additive DBE, indicating that the distinct π - π interaction induced by the planar and rigid configuration would prompt the molecular face-on fractions to a maximum amplitude, which is essential for high charge transport kinetics and further higher photovoltaic performance.³²

After detecting the horizontal direction, we further probed the crystallinity distribution and energetic disorder in the vertical direction by conducting angle-resolved GIWAXS measurement, which is a promising protocol to detect the inner crystallization information.³³ Indeed, the 2D GIWAXS diffraction patterns of the blend films with amplified incident angles (0.08° , 0.12° , and 0.20°) are displayed in Fig. S12 and S13 (ESI[†]), and corresponding line-cut profiles are demonstrated in Fig. 3d and e, respectively. As presented in Fig. 3f, which shows the summarized CCL values with respect to the incident angle, for the PM6:BTP-eC9 film casted using neat toluene solvent, the intensity of the scattering peaks varies obviously as the incident angle changes from 0.08° to 0.20° , and corresponding CCL values and d -spacing also demonstrate obviously different values with increasing incident angle, indicating that the bottom part near the anode demonstrates a closer molecular packing, while there is moderate crystallinity in the top region.³⁴ This uneven crystallinity can be attributed to the anisotropic orientation of the blend film, which is further major evidence of the severe energetic disorder in the neat-toluene-cast film.³⁵ However, π - π stacking peaks and the corresponding CCLs in the OOP direction show no obvious change for the PM6:BTP-eC9 blend film with DBE incorporation, suggesting the coherent crystallinity inside the blend film. This efficient manipulation triggered by the DBE treatment can inhibit the chaotic domain distribution and

facilitate the uniform crystallization in the vertical direction under thick-film conditions.³⁶

In addition to GIWAXS, the aggregation characteristics of the BHJ blend film can also be investigated using atomic force microscopy (AFM) measurement.³⁷ As shown in Fig. S14 (ESI[†]), due to the enhanced aggregation capability after the incorporation of aromatic DBE with strengthened intermolecular interaction, the PM6:BTP-eC9 film presents a root mean square (RMS) value of 1.65 nm with obvious phase contrast, whereas the dispersed acceptor induces a lower RMS value of 1.26 nm.³⁸

Based on the above discussion of the MD simulation, *in situ* spectroscopy and GIWAXS measurement results, an understanding of the effect of the SII methodology on the nano-micro structure in the blend film is proposed in Fig. 3g. The toluene-processed PM6:BTP-eC9 film demonstrates an anisotropic orientation with moderate molecular packing.³⁹ Conversely, the additive DBE, with the enhanced π - π interaction and hydrogen-bond effect, would act as a planar and rigid template on the BTP-eC9, which would trigger BTP-eC9 to pre-aggregate in the solution state and further transform into a more ordered packing with preferable alignment direction in the film state. This favorable blend morphology would activate the exciton and carrier dynamics and further enhance the photovoltaic performance of non-halogenated OSC devices.

Photovoltaic performance

Based on the merits discussed above, we subsequently constructed non-halogenated OSCs to explore the influence of the molecular framework of the ether additive on the photovoltaic performance. All devices were fabricated with the configuration ITO/2PACz/active layer/PNDI-F3N-Br/Ag (Fig. 4a). The representative current density–

voltage (J - V) curves and corresponding cell parameters, such as the short-circuit density (J_{sc}), open-circuit voltage (V_{oc}) and fill factor (FF) are shown in Fig. 4b and Table 1, respectively. The OSC based on neat toluene solvent was first fabricated as a reference, and the resulting device exhibited a champion PCE of 17.1%, with a J_{sc} of 25.7 mA cm^{-2} , V_{oc} of 0.87 V, and FF of 76.7%. After the incorporation of the additive DBE, the PCE value was enhanced to 19.4% with a remarkable J_{sc} of 28.0 mA cm^{-2} and FF of 80.5% as the concentration of DBE was increased from 0 to 0.5% volume ratio. Strikingly, as shown in Fig. 4c, in comparison with the PCE values from the literature, the 19.4% obtained through DBE treatment is one of the highest performance values among the non-halogenated OSC devices. Nevertheless, as shown in Table S3 (ESI[†]), there is a degradation of the PCE to 18.0% with further increasing the DBE ratio (1.0% DBE), suggesting that excessive additive is detrimental to device performance, especially the fill factor merit. We also sent one of our best cells to the authoritative third-party solar cell certification laboratory (SIMIT, China), where a certified PCE of 18.92% was achieved, suggesting the veracity of the performance result measured in our own laboratory (Fig. S15, ESI[†]).

To explore the enhancement of J_{sc} after the incorporation of DBE additive, the external quantum efficiency (EQE) curves were tested and are plotted in Fig. 4d. Specially, the EQE curve of the reference device based on neat toluene solvent displays a photoresponse window from 300–950 nm with EQE values of over 80% in the range from 500–800 nm. Interestingly, the enhanced π - π intermolecular interaction induced a red-shift trend with a higher EQE response, which is a obvious evidence

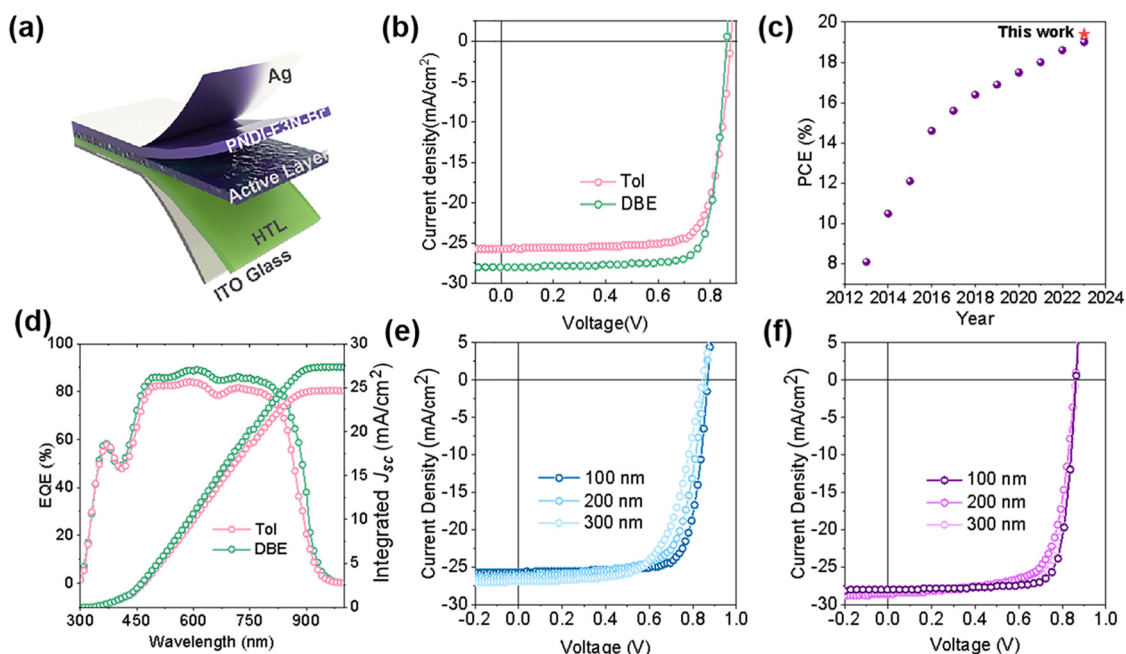


Fig. 4 (a) Schematic image of the device configuration. (b) J - V curves of PM6:BTP-eC9 without and with the additive DBE. (c) Summary of reported devices casted using non-halogenated solvents in the literature. (d) EQE curves of PM6:BTP-eC9 without and with the additive DBE. (e) J - V curves as a function of film thickness of the PM6:BTP-eC9 device without the ether additive. (f) J - V curves as a function of film thickness of PM6:BTP-eC9 device with the additive DBE.

Table 1 Summary of the figures of merit of the PM6:BTP-eC9 devices without and with the ether additive from 10 separated devices

Process	V_{oc} (V)	J_{sc} (mA cm^{-2})	FF (%)	PCE (%)
Tol	0.87 (0.86 \pm 0.01)	25.7 (23.7 \pm 1.9)	76.7 (74.3 \pm 2.3)	17.1 (16.8 \pm 0.3)
DBE	0.86 (0.85 \pm 0.01)	28.0 (26.8 \pm 1.2)	80.5 (78.7 \pm 1.9)	19.4 (19.1 \pm 0.3)

for the enhanced J_{sc} in the DBE device. These results clearly demonstrate that the SII strategy appreciably affects the aggregation of the BTP-eC9 acceptors and further photon-to-carrier conversion process through the critical π - π interaction. In addition, the integrated J_{sc} values were calculated to be 24.9 and 27.2 mA cm^{-2} for the toluene and DBE devices, respectively, which are in line with the J_{sc} values obtained from the J - V measurements with less than 5% discrepancy.

The processing method of commercial large-area OSCs requires the active layer to have a high tolerance for film thickness, that is, the efficiency of the device is negligibly affected by the change of film thickness. Therefore, the ability to achieve high efficiency under thick-film conditions is one of the necessary prerequisites for the realization of commercial organic solar cells.^{40,41} As uncontrollable aggregation would create an irregular molecular distribution underneath the active layer, the PCE values harvested using a BHJ layer treated with non-halogenated solvent normally present significant fluctuations under the altered film-thickness condition. Given the above investigation of the inhibited energetic disorder, it is natural to apply the superiority of the SII strategy to thick-film devices. The J - V curves and corresponding photovoltaic parameters with respect to the film thickness of the active layer are presented in Fig. 4e and f and Tables S4 and S5 (ESI[†]), respectively. Indeed, the photovoltaic performance yielded by

neat toluene solvent displays a continuous drop from 17.1% in 100 nm to 14.9% in 300 nm, while the slight J_{sc} increment from 25.7 mA cm^{-2} to 26.9 mA cm^{-2} in the 300 nm active layer devices are not enough to compensate for the FF loss (from 76.7% to 65.3%). In contrast, the DBE incorporation can remarkably slow the roll-off of the performance under the enhanced thickness, with the PCE being maintained at 17.4% for the active layer device when the thickness of active layer is increased to 300 nm, which is mainly ascribed to the sustainability of the FF parameter at a high level (72.3%) when the thickness is increased to 300 nm, suggesting the SII strategy can ameliorate the inferior crystallinity kinetics due to the non-halogenated solvent for up-scaled fabrication of eco-friendly OSCs.⁴²

We also tested the universality of the additive DBE in distinct solvents, such as the classic solvents chloroform (CF) and chlorobenzene (CB). As shown in Fig. S16 and Tables S6 and S7 (ESI[†]), J_{sc} and FF were significantly improved with the addition of DBE additives in CF and CB solvent, suggesting the good generality of this DBE additive in various working solvent systems.

Optoelectronic characterization

Femtosecond transient absorption (fs-TA) was first implemented to analyze the exciton dynamics after the SII treatment.⁴³ Upon pumping with a 800 nm pulse, as shown in Fig. 5a and c,

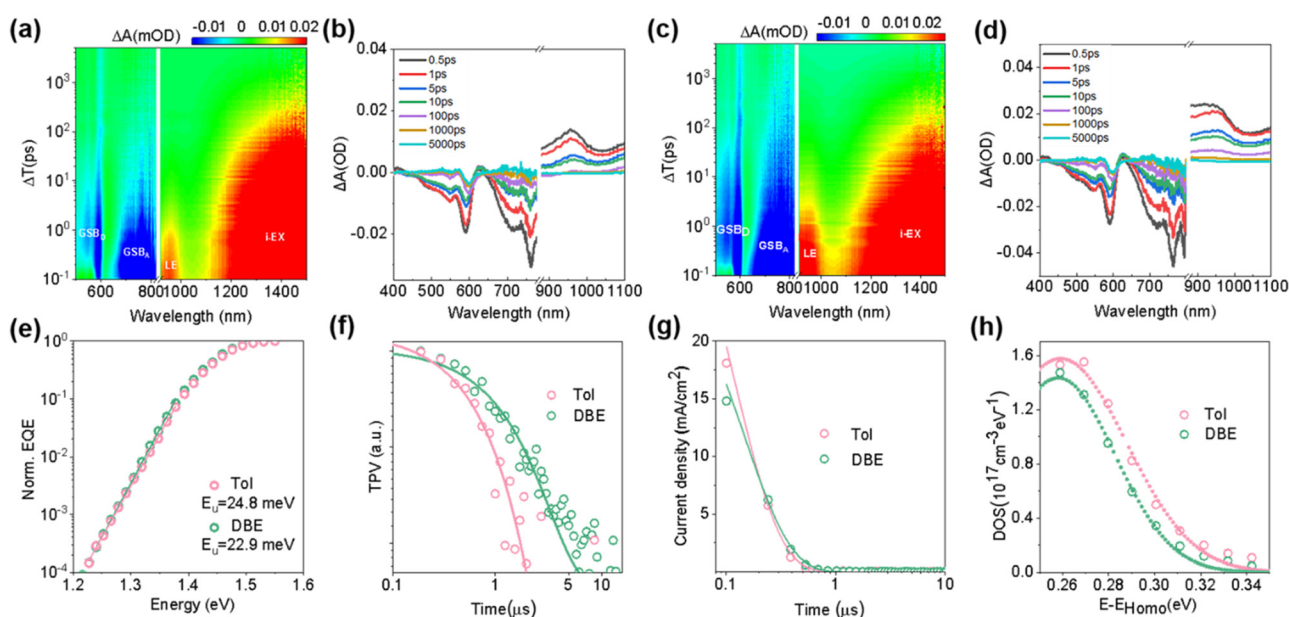


Fig. 5 2D TA mapping of PM6:BTP-eC9 without (a) and with the additive DBE (c) under 800 nm excitation. TA curves with different decay times of PM6:BTP-eC9 without (b) and with the additive DBE (d) under 800 nm excitation. (e) s-EQE curves of PM6:BTP-eC9 devices without and with the additive DBE. (f) TPV curves of PM6:BTP-eC9 without and with the additive DBE. (g) DLTS curves of PM6:BTP-eC9 without and with the additive DBE. (h) DOS curves of PM6:BTP-eC9 without and with the additive DBE.

the toluene and DBE treated films presented ground-state bleaching (GSB) of PM6 at ~ 600 nm, which is in accordance with the previous conclusion of a hole-transfer process. To move forward, as shown in Fig. S17 (ESI[†]), we fitted the decay curves using a biexponential function to evaluate the hole transfer rate, where τ_1 and τ_2 represent the rapid exciton dissociation at the donor-acceptor (D-A) interface and exciton diffusion toward the D-A interface. Interestingly, the toluene- and DBE-treated blend films demonstrate τ_1 values of 0.46 and 0.35 ps, respectively, while the τ_2 values are 7.53 and 6.18 ps, respectively. These results obviously demonstrate that the manipulated blend morphology can accelerate the hole transfer kinetics and further enhance the carrier generation efficiency.⁴⁴

To further evaluate the exciton generation rate after the SII treatment, film-depth-dependent light absorption spectroscopy (FLAS) measurement was applied. According to the absorption spectrum with respect to the film thickness (Fig. S18, ESI[†]), the exciton generation contours at each film-depth were systematically simulated from FLAS in combination with the optical matrix-transfer model. As shown in Fig. S19 and S20 (ESI[†]), due to the higher crystalline phases (confirmed by GIWAXS patterns), a higher exciton generation region, especially in the acceptor part (700–900 nm), is apparent after the DBE additive treatment. More vitally, the maximum exciton generation rate (G_{\max}) value is significantly strengthened from $16.2 \text{ nm}^{-3} \text{ s}^{-1}$ to $19.7 \text{ nm}^{-3} \text{ s}^{-1}$ after the molecular configuration modification, which is one of the major impacts for the accelerated J_{sc} value in the corresponding devices.

To explore the significant improvement of the FF (from 76.7% to 80.5%) with the addition of DBE, the sensitive EQE (s-EQE) spectrum was characterized to calculate the Urbach energy (E_{u}) parameter and determine the energetic disorder tendency.⁴ The E_{u} can be extracted using eqn (1):

$$\alpha(E) = \alpha_0 e^{\frac{E-E_{\text{g}}}{E_{\text{u}}}}, \quad (1)$$

where $\alpha(E)$ is the optical absorption coefficient, α_0 and E_{g} are constants, and E is the photon energy.

By fitting the sub-bandgap s-EQE plots with a natural logarithm decay, as presented in Fig. 5e, an E_{u} of 24.8 meV is extracted from the neat-toluene-casted device, whereas the DBE device exhibits a reduced energetic disorder with an E_{u} of 22.9 meV. This reduced energetic disorder could be caused by highly crystallinity with enlarged CCL as measured in the GIWAXS characterizations, indicating enhanced charge-transportation capability after the incorporation of DBE, which is in line with the increased FF.⁴⁵

The energetic disorder is reliably related to the carrier mobility, which is a critical factor in the carrier transport kinetics. Subsequently, the space-charge limited current (SCLC) method was applied to evaluate the hole (u_{h}) and electron (u_{e}) mobilities of the PM6:BTP-eC9 blend films after either additive incorporation. The J - V curves of the hole-only and electron-only devices are plotted in Fig. S21 and S22 (ESI[†]), respectively. The as-cast toluene blend films showed u_{h} values of $1.60 \times 10^{-4} \text{ cm}^2 \text{ V}^{-1} \text{ s}^{-1}$ and u_{e} values of $0.80 \times 10^{-4} \text{ cm}^2 \text{ V}^{-1} \text{ s}^{-1}$,

giving a $u_{\text{h}}/u_{\text{e}}$ ratio of 2.0. The DBE additive incorporation is beneficial for the enhancement of the crystallinity of the PM6:BTP-eC9 blend films.⁴⁴ A higher u_{e} value of $1.61 \times 10^{-4} \text{ cm}^2 \text{ V}^{-1} \text{ s}^{-1}$ together with an elevated u_{h} of $1.64 \times 10^{-4} \text{ cm}^2 \text{ V}^{-1} \text{ s}^{-1}$ are achieved in the DBE-based system, leading to more balanced transport with a $u_{\text{h}}/u_{\text{e}}$ ratio of 1.0, implying that the finely manipulated aggregation initiated by the π - π interaction can preferentially optimize the carrier transport channel in the active layer, which is vital for the improvement of the FF parameter in the corresponding device.

In addition to the charge transport kinetics, the charge recombination behavior is critical to the J_{sc} and FF merits. To elucidate the charge recombination diversity, the dependence of J_{sc} and V_{oc} on the light intensity (P_{light}) of the devices is investigated. The slope between J_{sc} and P_{light} is a signal of bimolecular recombination. As depicted in Fig. S23 (ESI[†]), the slopes between $J_{\text{sc}}-P_{\text{light}}$ were close to unity in the Tol and DBE devices, indicating negligible bimolecular recombination. Additionally, the correlation between V_{oc} and P_{light} follows the equation $V_{\text{oc}} \propto n(kT/q) \ln P_{\text{light}}$, where k , q and T refer to the Boltzmann constant, elementary charge, and Kelvin temperature. As depicted in Fig. S24 (ESI[†]), the slope declines from 1.68 kT/q (Tol device) to 1.21 kT/q (DBE device), indicating much less trap-assisted recombination after the incorporation of the aromatic additive DBE. Moreover, the transient photovoltage (TPV) was measured to distinguish the carrier lifetime after DBE incorporation, which is another signal of the carrier recombination potential. As illustrated in Fig. 5f, the DBE device possesses a lifetime of 4.36 μs , which is much longer than its control counterpart (2.57 μs), indicating reduced recombination loss in the DBE-treated device.

The suppressed recombination is in good accordance with the reduced trap density (N_{t}), which can be detected by current-based deep level transient spectroscopy (DLTS) measurement as described in formula (2):

$$j_{\text{te}} = \frac{1}{\tau_{\text{te}}} q d N_{\text{t}} \exp\left(-\frac{t}{\tau_{\text{te}}}\right) \quad (2)$$

Here, τ_{te} is the trap emission time constant, q is the elementary charge, d represents the device thickness (or the depletion width in thick devices), and N_{t} is the trap volume density.⁴⁶ Therefore, as shown in Fig. 5g, the N_{t} value decreased from $2.4 \times 10^{16} \text{ cm}^{-3}$ to $1.4 \times 10^{16} \text{ cm}^{-3}$ after the addition of DBE, demonstrating that the morphology regulation by the planar and rigid additive DBE can effectively inhibit the inner non-radiative recombination. Taken together, these results reveal the suppressed traps and diminished energetic disorder achieved using this SII strategy, which could effectively facilitate the electron delocalization and subsequently promote the carrier kinetics.

The diminished trap density can also be quantitatively and accurately measured through density of states (DOS) measurements. From the capacitance-frequency (C - f) and forward-bias capacitance-voltage (C - V) measurements (Fig. S25 and S26, ESI[†]), the trap density can be fitted using Walter's model as

follows in eqn (3):⁴⁷

$$N_t(E) = \frac{N_t}{\sqrt{2\pi}\delta} \exp\left(-\frac{(E_t - E)^2}{2\delta^2}\right), \quad (3)$$

where N_t is the total density (cm^{-3}), E_t is the center of the density of states (DOS), and δ is the disorder parameter. As presented in Fig. 5h, the enhanced crystallinity and adjusted energetic disorder with DBE incorporation clearly correlate to the lower N_t value (Tol: $1.56 \times 10^{16} \text{ cm}^{-3}$, DBE: $1.21 \times 10^{16} \text{ cm}^{-3}$), which is in line with the tendency measured using DLTS characterization.

Furthermore, transient photocurrent (TPC) measurement was applied to qualify the carrier extraction process after the SII treatment. As shown in Fig. S27 (ESI[†]), the DBE-based device exhibits a shorter charge extraction time of 0.68 μs than that of the toluene-casted device (0.92 μs). In short, these results illustrate that the strengthened intermolecular interaction approach can reinforce the accelerated carrier extraction dynamics.⁴⁷ Therefore, according to these systemic morphological and transient optoelectronic characterizations, we can conclude that the π - π interaction after the DBE additive incorporation would induce the pre-aggregation of the acceptor molecule and further re-assemble the blend morphology. This favorable blend morphology leads to the lower energetic disorder, diminished trap density and prolonged carrier transport capability, thus yielding a higher FF and J_{sc} in the DBE device.⁴⁸

3. Conclusion

In conclusion, a strengthened intermolecular interaction approach to construct efficient non-halogenated OSCs has been presented. We discovered that the aromatic additive DBE could induce dual-functional hydrogen-bond and π - π interactions with the acceptor and trigger an enhanced polycrystalline crystallinity structure. In particular, this SII strategy can induce the acceptor molecules to form pre-aggregation in the solution state and construct a tight and preferential molecular aggregation structure. This reorganized morphology manipulation is beneficial for enhancing the J_{sc} and FF parameters by inhibiting the trap density and energetic disorder capability. As a result, the apparently high efficiency (19.4%) is harvested with the assistance of this SII strategy, which is one of the highest performances for non-halogenated OSC devices. Our work suggests that the incorporation of a planar and rigid additive is a promising strategy for retarding the energetic disorder loss and further constructing efficient non-halogenated OSC devices.

Author contributions

S. G and Y. Z. contributed equally to this work. X. S. conceived the idea and designed the overall experiments. S. G., X. H., X. Z. and X. S. prepared the device. Y. Z., D. C. and S. M. performed the simulation. S. J. and C. Y. performed the GIWAXS measurement. X. S. wrote the manuscript. C. Y., S. M. W. L and W. Z. revised the manuscript. X. S. led and supervised the whole research project.

Data availability

All data needed to evaluate the conclusions in the paper have been included as part of the ESI.[†]

Conflicts of interest

There are no conflicts to declare.

Acknowledgements

We gratefully express our thanks for the financial support from National Natural Science Foundation of China (62105129, 12025407, 12304351, 11934004).

References

- 1 L. Zhu, M. Zhang, J. Xu, C. Li, J. Yan, G. Zhou, W. Zhong, T. Hao, J. Song, X. Xue, Z. Zhou, R. Zeng, H. Zhu, C.-C. Chen, R. C. I. MacKenzie, Y. Zou, J. Nelson, Y. Zhang, Y. Sun and F. Liu, *Nat. Mater.*, 2022, **21**, 656.
- 2 X. Xu, G. Zhang, L. Yu, R. Li and Q. Peng, *Adv. Mater.*, 2019, **31**, 1906045.
- 3 L. Hong, H. Yao, Z. Wu, Y. Cui, T. Zhang, Y. Xu, R. Yu, Q. Liao, B. Gao, K. Xian, H. Y. Woo, Z. Ge and J. Hou, *Adv. Mater.*, 2019, **31**, 1903441.
- 4 X. Song, H. Xu, X. Jiang, S. Gao, X. Zhou, S. Xu, J. Li, J. Yu, W. Liu, W. Zhu and P. Müller-Buschbaum, *Energy Environ. Sci.*, 2023, **16**, 3441.
- 5 H. Zhao, J. Xue, H. Wu, B. Lin, Y. Cai, K. Zhou, D. Yun, Z. Tang and W. Ma, *Adv. Funct. Mater.*, 2020, **30**, 1908336.
- 6 X. Cai, X. Wang, Y. Ma, D. Shen, H. Deng, T. Zhang, J. Wang, J. Zhang, R. Li, L. Wang, Q. Zhang, Z. Cheng, H. Zhang, C. Zhou, Z. Tian and Z. Wei, *Joule*, 2023, **7**, 2386.
- 7 J. Zhao, Y. Li, G. Yang, K. Jiang, H. Lin, H. Ade, W. Ma and H. Yan, *Nat. Energy*, 2014, **1**, 15027.
- 8 Y. Zhang, H. Feng, L. Meng, Y. Wang, M. Chang, S. Li, Z. Guo, C. Li, N. Zheng, Z. Xie, X. Wan and Y. Chen, *Adv. Energy Mater.*, 2019, **9**, 1902688.
- 9 D. Liu, B. Kan, X. Ke, N. Zheng, Z. Xie, D. Lu and Y. Liu, *Adv. Energy Mater.*, 2018, **8**, 1801618.
- 10 H. Chen, R. Zhang, X. Chen, G. Zeng, L. Kobera, S. Abbrent, B. Zhang, W. Chen, G. Xu, J. Oh, Y. Li and Y. Li, *Nat. Energy*, 2021, **6**, 1045.
- 11 S. Dong, T. Jia, K. Zhang, J. Jing and F. Huang, *Joule*, 2020, **4**, 2004.
- 12 Z. Zhong, S. Chen, J. Zhao, J. Xie, K. Zhang, T. Jia, C. Zhu, J. Jing, Y. Liang, L. Hong, S. Zhu, D. Ma and F. Huang, *Adv. Energy Mater.*, 2023, **13**, 2302273.
- 13 Y. Wei, Y. Cai, X. Gu, G. Yao, Z. Fu, Y. Zhu, J. Yang, J. Dai, J. Zhang, X. Zhang, X. Hao, G. Lu, Z. Tang, Q. Peng, C. Zhang and H. Huang, *Adv. Mater.*, 2023, **36**, 2304225.
- 14 B. R. Luginbuhl, P. Raval, T. Pawlak, Z. Du, T. Wang, G. Kupgan, N. Schopp, S. Chae, S. Yoon, A. Yi and H. J. Kim, *Adv. Mater.*, 2022, **34**, 2105943.

- 15 Z. Li, L. Ying, P. Zhu, W. Zhong, N. Li, F. Liu, F. Huang and Y. Cao, *Energy Environ. Sci.*, 2019, **12**, 157.
- 16 X. Song, K. Zhang, R. Guo, K. Sun, Z. Zhou, S. Huang, L. Huber, M. Reus, J. Zhou, M. Schwartzkopf, S. V. Roth, W. Liu, Y. Liu, W. Zhu and P. Müller-Buschbaum, *Adv. Mater.*, 2022, **34**, 2200907.
- 17 D. Li, L. Wang, C. Guo, Y. Liu, B. Zhou, Y. Fu, J. Zhou, D. Liu, W. Li and T. Wang, *ACS Mater. Lett.*, 2023, **5**, 2065.
- 18 G. Zhang, X. Chen, J. Xiao, C. Chow, M. Ren, G. Kupgan, X. Jiao, C. Chan, X. Du, R. Xia, Z. Chen, H. Yip and Y. Cao, *Nat. Commun.*, 2020, **11**, 3943.
- 19 S. Jeong, J. Park, Y. Ji, Y. Cho, B. Lee, M. Jeong, S. Jung, S. Yang, Y. Zhang, S. J. Yoon and C. Yang, *J. Mater. Chem. A*, 2023, **11**, 4703.
- 20 X. Song, Y. Song, H. Xu, S. Gao, Y. Wang, J. Li, J. Hai, W. Liu and W. Zhu, *Adv. Energy Mater.*, 2023, **13**, 2203009.
- 21 R. Ma, C. Yan, W. Fong, J. Yu, H. Liu, J. Yin, J. Huang, X. Lu, H. Yan and G. Li, *Energy Environ. Sci.*, 2022, **15**, 2479.
- 22 M. Ghasemi, N. Balar, Z. Peng, H. Hu, Y. Qin, T. Kim, J. J. Rech, M. Bidwell, W. Mask, I. McCulloch, W. You, A. Amassian, C. Risko, B. T. O'Connor and H. Ade, *Nature Mater.*, 2021, **20**, 525.
- 23 W. Xue, Z. Liang, Y. Tang, C. Zhao, L. Yan, W. Ma and H. Yan, *Adv. Funct. Mater.*, 2023, **33**, 2304960.
- 24 Y. Liu, Q. Fan, H. Liu, I. Jalan, Y. Jin, J. v Stam, E. Moons, E. Wang, X. Lu, O. Inganäs and F. Zhang, *J. Phys. Chem. Lett.*, 2022, **13**, 11696.
- 25 M. Sun, K. Zhang, J. Qiao, L. Wang, M. Li, P. Lu, W. Qin, Z. Xiao, L. Zhang, X. Hao, L. Ding and X. Du, *Adv. Energy Mater.*, 2023, **13**, 2203465.
- 26 K. Hu, C. Zhu, K. Ding, S. Qin, W. Lai, J. Du, J. Zhang, Z. Wei, X. Li, Z. Zhang, L. Meng, H. Ade and Y. Li, *Energy Environ. Sci.*, 2022, **15**, 4157.
- 27 Y. Shen, H. Zhang, J. Zhang, C. Tian, Y. Shi, D. Qiu, Z. Zhang, K. Lu and Z. Wei, *Adv. Mater.*, 2023, **35**, 2209030.
- 28 D. Baran, R. S. Ashraf, D. A. Hanifi, M. Abdelsamie, N. Gasparini, S. Holliday, S. Lockett, M. Neophytou and I. McCulloch, *Nat. Mater.*, 2017, **16**, 363.
- 29 Y. Wei, Z. Chen, G. Lu, N. Yu, C. Li, J. Gao, X. Gu, X. Hao, G. Lu, Z. Tang, J. Zhang, Z. Wei, X. Zhang and H. Huang, *Adv. Mater.*, 2022, **34**, 2204718.
- 30 T. Liu, W. Gao, Y. L. Wang, T. Yang, R. J. Ma, G. Y. Zhang, C. Zhong, W. Ma, H. Yan and C. L. Yang, *Adv. Funct. Mater.*, 2019, **29**, 1902155.
- 31 P. Müller-Buschbaum, *Adv. Mater.*, 2014, **26**, 7692.
- 32 T. Xia, Y. Cai, H. Fu and Y. Sun, *Sci. China Chem.*, 2019, **62**, 662.
- 33 H. Zhao, J. Xue, H. Wu, B. Lin, Y. Cai, K. Zhou, D. Yun, Z. Tang and W. Ma, *Adv. Funct. Mater.*, 2023, **33**, 2210534.
- 34 J. Xue, H. Zhao, B. Lin, Y. Wang, Q. Zhu, G. Lu, B. Wu, Z. Bi, X. Zhou, C. Zhao, G. Lu, K. Zhou and W. Ma, *Adv. Mater.*, 2022, **34**, 2202659.
- 35 Y. Yu, R. Sun, T. Wang, X. Yuan, Y. Wu, Q. Wu, M. Shi, W. Yang, X. Jiao and J. Min, *Adv. Funct. Mater.*, 2021, **31**, 2008767.
- 36 S. Bao, H. Yang, H. Y. Fan, J. Q. Zhang, Z. X. Wei and C. Cui, *Adv. Mater.*, 2021, **33**, 2105301.
- 37 X. Xu, Y. Li and Q. Peng, *Adv. Mater.*, 2021, **34**, 2107476.
- 38 C. Guan, C. Xiao, X. Liu, Z. Hu, R. Wang, C. Wang, C. Xie, Z. Cai, W. Li and Y. Sun, *Angew. Chem., Int. Ed.*, 2023, **62**, e202312357.
- 39 L. Zhan, S. Yin, X. Zhan, Y. Li, S. Li, T. Chen, R. Sun, J. Min, G. Zhou, H. Zhu, Y. Chen, J. Fang, C.-Q. Ma, X. Xia, X. Lu, H. Qiu, W. Fu and H. Chen, *Adv. Mater.*, 2022, **34**, 2206269.
- 40 G. Zhang, K. Zhang, Q. Yin, X.-F. Jiang, Z. Wang, J. Xin, W. Ma, H. Yan, F. Huang and Y. Cao, *J. Am. Chem. Soc.*, 2017, **139**, 2387.
- 41 Y. Cai, Q. Li, G. Lu, H. S. Ryu, Y. Li, H. Jin, Z. Chen, Z. Tang, G. Lu, X. Hao, H. Y. Woo, C. Zhang and Y. Sun, *Nature Commun.*, 2022, **13**, 2369.
- 42 N. Camaioni, C. Carbonera, L. Ciammaruchi, G. Corso, J. Mwaura, R. Po and F. Tinti, *Adv. Mater.*, 2023, **35**, 2210146.
- 43 J. Wu, J. Lee, Y.-C. Chin, H. Yao, H. Cha, J. Luke, J. Hou, J.-S. Kim and J. R. Durrant, *Energy Environ. Sci.*, 2020, **13**, 2422.
- 44 P. Bi, S. Zhang, Z. Chen, Y. Xu, Y. Cui, T. Zhang, J. Ren, J. Qin, L. Hong, X. Hao and J. Hou, *Joule*, 2021, **5**, 2408.
- 45 J. Yuan, C. Zhang, B. Qiu, W. Liu, S. K. So, M. Mainville, M. Leclerc, S. Shoaee, D. Neher and Y. Zou, *Energy Environ. Sci.*, 2022, **15**, 2806.
- 46 J. Zhao, S. Chung, H. Li, Z. Zhao, C. Zhu, J. Yin, K. Cho and Z. Kan, *Adv. Funct. Mater.*, 2023, **33**, 2307355.
- 47 S. Khelifi, K. Decock, J. Lauwaert, H. Vrielinck, D. Spoltore, F. Piersimoni, J. Manca, A. Belghachi and M. Burgelman, *J. Appl. Phys.*, 2011, **110**, 094509.
- 48 Z. Zhang, D. Deng, Y. Li, J. Ding, Q. Wu, L. Zhang, G. Zhang, M. J. Iqbal, R. Wang, J. Zhang, X. Qiu and Z. Wei, *Adv. Energy Mater.*, 2022, **12**, 2102394.